HHS Public Access

Author manuscript

Photochem Photobiol. Author manuscript; available in PMC 2023 March 24.

Published in final edited form as:

Photochem Photobiol. 2022 January ; 98(1): 220–231. doi:10.1111/php.13501.

Dual Function Antibody Conjugates for Multimodal Imaging and Photoimmunotherapy of Cancer Cells

Mohammad A. Saad[1], **Marvin Xavierselvan**[2], **Hamza A. Sharif**[3], **Scott Selfridge**[4], **Robert Pawle**[4], **Mark Varvares**[5], **Srivalleesha Mallidi**[1,2], **Tayyaba Hasan**[1,6,*]

[1]Wellman Center for Photomedicine, Massachusetts General Hospital, Harvard Medical School, Boston, MA

[2]Department of Biomedical Engineering, Science and Technology Center, Tufts University, Medford, MA

[3]Albany Medical College, Albany, NY

[4]Akita Innovations, North Billerica, MA

[5]Department of Otolaryngology Head and Neck Surgery, Harvard Medical School, The Massachusetts Eye and Ear, Boston, MA

[6]Division of Health Sciences and Technology, Harvard University and Massachusetts Institute of Technology, Cambridge, MA

Abstract

Precision imaging, utilizing molecular targeted agents, is an important tool in cancer diagnostics and guiding therapies. While there are limitations associated with single mode imaging probes, multimodal molecular imaging probes enabling target visualization through complementary imaging technologies provides an attractive alternative. However, there are several challenges associated with designing molecular probes carrying contrast agents for complementary multi-modal imaging. Here, we propose a dual function antibody conjugate (DFAC) comprising an FDA approved photosensitizer Benzoporphyrin derivative (BPD) and a naphthalocyanine-based photoacoustic dye (SiNc(OH)) for multimodal infrared (IR) imaging. While fluorescence imaging, through BPD, provides sensitivity, complementing it with photoacoustic imaging, through SiNc(OH), provides a depth-resolved spatial resolution much beyond the optical diffusion limits of fluorescence measurements. Through a series of in vitro experiments, we demonstrate the development and utilization of DFACs for multimodal imaging and photodynamic treatment of squamous cell carcinoma (A431) cell line. The proposed DFACs have potential use in precision imaging applications such as guiding tumor resection surgeries and photodynamic treatment of residual microscopic disease thereby minimizing local recurrence. The data demonstrated in this study merits further investigation for its preclinical and clinical translation.

[*]Corresponding author thasan@mgh.harvard.edu (Tayyaba Hasan).

CONFLICT OF INTEREST

Scott Selfridge andRobert Pawle are full time employees of Akita Innovations, LLC, a provider ofcustom designed bioimag-ing dyes. All other authors declare no competing financial inter-est.

INTRODUCTION

Multimodal real-time precision imaging is a promising approach for diagnostics, treatment guidance, and treatment monitoring applications in cancer management (1-3). In this context, real-time imaging by white light reflectance, fluorescence, and ultrasound imaging holds an advantage over MRI, CT, X-ray, etc., which do not provide real-time feedback and are mostly used for interim assessment (4). While fluorescence and reflectance imaging hold an advantage owing to their higher microscopic resolution, the depth profiling conferred by these imaging modalities is often low; a shortcoming easily compensated by acoustic contrast imaging (5). Multimodal imaging technologies comprising fluorescence and photoacoustic imaging (PAI) may thus provide a better spatial resolution well beyond the depth penetration limits of fluorescence imaging (6-9). Importantly, while fluorescence imaging is FDA approved for cancer diagnosis, surveillance and guiding resection surgeries (10), PA imaging has been making its mark in the clinical realm (11) with a recently granted premarket approval from FDA for breast cancer imaging (NCT03897270).

Most externally administered fluorophores and sonochromes used for enhancing contrast in fluorescence and PA imaging, respectively, have limitations owing to their nonspecific accumulation and often lead to nonspecific false positive signals, which compromises their use as contrast agents (12,13). Most contrast agents rely on enhanced permeability and retention (EPR) (14) based accumulation in tumor sites and often lead to low signal-to-noise ratios. A major improvement over this has been the development of targeted imaging probes, which have shown success in enhancing signal to noise ratio in several preclinical and clinical studies (15). Several molecular markers have been identified and used for diagnosis and therapeutic targeting in various tumor types, both in preclinical and clinical studies with fluorescence and photoacoustic imaging (16-18). These include Folate receptor (19), EGFR (20,21), HER2 (22), cathepsins (23), and MMPs (4,24,25). EGFR over-expression is the hallmark of several tumors and EGFR-targeted antibodies have thus been widely used for molecular imaging to guide surgical resection and treatment in several tumor types including head and neck cancers, gliomas, pancreatic cancers, and lung cancers (21, 26-30,). Another advantage of using molecular targeted agents in multi-modal imaging is the simultaneous delivery of multiple contrast agents at the “right-place right-time,” thus achieving the desired contrast for multimodal imaging.

Interestingly, most of the FDA approved fluorophores (methylene blue (MB), indocyanine green (ICG) (31) and the nonfluorescent pro-drug; ALA) (32) are photosensitizers and can be used for treatment through photodynamic therapy (PDT) (33), as successfully demonstrated both preclinically and clinically (34). In this study, we report the synthesis and characterization of a multimodal imaging probe for possible use in detection and treatment of EGFR-positive tumors. We use a naphthalocyanine derived PA contrast agent (SiNc(OH)) along with Benzoporphyrin derivative (BPD; a photosensitizer), conjugated to Cetuximab antibody to achieve target-specific multimodal imaging. Naphthalocyanine based dyes have been used as sonochromes and also as photosensitizing agents (35,36). Their absorption maxima may vary from 750 to 940 nm, depending on the substitution on the tetrapyrrolic π-system and the central metal atom (37). Benzoporphyrin derivative (BPD) was chosen for its fluorescence and photosensitizing properties. We have previously demonstrated the

synthesis of BPD-based photoimmunoconjugates and application in imaging and targeted PDT (photoim-munotherapy) of different tumor types (38). Overall, this study demonstrates the development and *in vitro* application of BPD and SiNc(OH)-conjugated Cetuximab, referred to as "Dual Function Antibody Conjugate (DFAC)" (39,40), to enhance imaging sensitivity and specificity for diagnosis and photodynamic therapy of EGFR overexpressing tumor cells.

MATERIALS AND METHODS

Synthesis of Naphthalocyanine derivative (SiNc(OH)) and its NHS derivative (SiNc(OH)-NHS).

All synthetic transformations were performed under an argon atmosphere with magnetic stirring unless otherwise mentioned. Flash chromatography was performed using a CombiFlash with RediSep pre-packed silica columns (230-400 mesh) as the stationary phase, unless otherwise stated. NMR spectra were acquired on a Varian 400 MHz Unity Inova spectrometer. Chemical shifts are reported relative to residual protonated solvent (7.26 ppm for $CHCl_3$). All reagents were purchased from Sigma-Aldrich, TCI, Santa Cruz Biotech, Gelest, or other commercial suppliers and used as received unless otherwise stated. Preparation of compounds 2 and 3 (Fig. 1) is described by Aouida *et al.* (37). Preparation of 3 was based on established procedures of analogous compounds (41). We prepared 1 from 3 using a large excess of suberic acid bis(N-hydroxysuccinimidylester) to minimize dimerization.

Preparation of silicon 1,6,10,15,19,24,28,33-octabutoxy-2,3-naphthalocyanine monohydroxide mono(3'-aminopropyl)dimethylsiloxide (SiNc(OH) (4).

A 50 mL round bottom flask equipped with a short path distillation unit was charged with 59 mg (0.04 mmol) silicon 1,6,10,15,19,24,28,33-octabutoxy-2,3-naphthalocyanine dihydroxide (**3**). 10 mL of pyridine was added to the reaction vessel and the mixture was stirred and sparged with argon for 5 min. 67 mg (0.45 mmol) of 3'-aminopropyldimethylmethoxysilane was dissolved in 10 mL of pyridine (0.05 M solution) and 1.0 mL (0.08 mmol) of the above solution was added to the reaction vessel. The mixture was sparged with argon for 10 min and then heated to 135 °C. The mixture was stirred for 1.5 h and the reaction temperature was increased to 170 °C and heated until approximately 3 mL of pyridine had distilled (~1 h). The mixture was cooled to room temperature and transferred to a single neck round bottom flask by rinsing with toluene. The solvent was removed *in vacuo*, and the solid was dissolved in dichloromethane and immobilized on sand. The crude product was purified by CombiFlash chromatography using amine gold NH_2-functionalized silica, 7:3 hexane:dichloromethane. The relevant fractions were combined, and the solvent was removed *in vacuo* yielding 18.8 mg (31.3%) of SiNc(OH) (**4**), a brown crystalline powder. ^{1}H NMR ($CDCl_3$, 400 MHz) δ: 9.00 (m, 8H), 7.91 (m, 8H), 5.20 (t, J = 7 Hz, 16H), 2.24 (m, 16H), 1.66 (sextet, J = 8 Hz, 16H), 1.04 (t, J = 7 Hz, 24H), 0.89 (m, 2H), −0.59 (m, 2H), −1.66 (m, 2H), −2.21 (s, 6H).

Preparation of silicon 1,6,10,15,19,24,28,33-octabutoxy-2,3-naphthalocyanine monohydroxide mono(3'-propyl(suberic acid amide mono(N-hydroxysuccinimidyl ester))dimethylsiloxide (SiNc(OH)-NHS) (1).

A 20 mL scintillation vial was charged with 18.6 mg (0.01 mmol) of SiNc(OH) (**4**) (Fig. 1). 10 mL dichloromethane was added to the reaction mixture and the mixture was sparged with argon for 5 min. 96.4 mg (0.26 mmol) suberic acid bis(*N*-hydroxysuccinimidyl ester) and 0.1 mL triethylamine were added to the reaction vessel and the mixture stirred for 16 h at room temperature. The solvent was removed *in vacuo* and the crude product was immobilized on sand. The product was purified using CombiFlash chromatography on silica with gradient elution (dichloromethane to 2% ethanol in dichloromethane). The appropriate fractions were collected, and the solvent was removed *in vacuo*. A white powder impurity was observed in the product, so the solid was redissolved in 1 mL of dichloromethane and the white impurity was precipitated with hexanes. The mixture was centrifuged, and the supernatant was saved. The pellet was redissolved in dichloromethane, and the hexanes precipitation/centrifugation was repeated. The supernatants were combined, and the solvents were removed *in vacuo* yielding 11.2 mg (50.5%) SiNc (OH)-NHS (**1**), a brown crystalline powder. ^{1}H NMR ($CDCl_3$, 400 MHz) δ: 9.00 (m, 8H), 7.92 (m, 8H), 5.19 (m, 16H), 2.83 (s, 4H), 2.24 (m, 20H), 1.65 (m, 20H), 1.25 (m, 4H), 1.03 (t, J = 7 Hz, 24H), 0.89 (m, 2H), −0.67 (m, 2H), −1.58 (m, 2H), −2.21 (s, 6H).

Dual function antibody conjugate (DFAC) synthesis.

Erbitux (human anti-EGFR antibody; Cetuximab) was obtained from Eli Lilly and Co. (Indianapolis, IN). The antibody was filtered under sterile conditions by passing through a 0.22 μm syringe filter. The concentration of the antibody was estimated using a Pierce™ BCA Protein Assay Kit (Thermo Fisher Scientific, Waltham, MA). 2 mL of antibody corresponding to ~4 mg was obtained in a scintillation vial and 0.2 mL of 4 mg mL^{-1} Methoxy PEG Succinimidyl Carbonate, (MW 10000) (JenKem Technology, Plano, TX), dissolved in DMSO, was added drop wise under stirring. The reaction was left over night at room temperature under stirring. SiNc(OH)-NHS and BPD-NHS (at 4 times molar excess), dissolved in DMSO, were added dropwise to the PEGylated antibody and the reaction was allowed to proceed for 4 h. The total DMSO content in the reaction mix was never allowed to exceed 40%. The reaction mix was centrifuged for 10 min at 15 000 ***g*** to remove any insoluble aggregates formed during the reaction. The supernatant containing the crude DFAC was passed through a Zeba™ Spin Desalting Column (7K MWCO, 10 mL) (Thermo Fisher Scientific, Waltham, MA) pre-equilibrated with 30% DMSO. The eluent obtained after passing through the gel filtration column was then subjected to buffer exchange and concentrated using a 30 kDa NMWL Amicon® Ultra-15 Centrifugal Filter Unit Amicon filter (MilliporeSigma, Burlington, MA). The final DMSO content of the DFAC was approximately 5%. DFACs were stored at 4°C and remained stable for months.

Estimation of BPD and SiNc(OH) molar loading ratios in DFACs.

Absorption spectra of DFAC was recorded, at appropriate dilutions in DMSO, using an Evolution™ 300 UV-Vis Spectrophotometer (Thermo Fisher Scientific). Absorbance at 687 nm and 865 nm was recorded, and the respective concentrations of BPD (34 895 $M^{-1}cm^{-1}$)

and SiNc(OH) (190 000 $M^{-1}cm^{-1}$) were calculated using their extinction coefficients in DMSO. The concentration of the Cetuximab antibody was calculated using a Pierce™ BCA Protein Assay Kit (Thermo Fisher Scientific, Waltham, MA). The loading ratios and conjugation efficiencies of the two dyes were subsequently calculated using the obtained concentrations of the dyes and protein (antibody), respectively.

Photophysical characterization of DFACs.

Comparative fluorescence studies for free BPD and DFAC were performed using a SpectraMax M5 multimode microplate reader (Molecular Devices, San Jose, CA). BPD (stock prepared in DMSO) and DFACs were diluted in PBS at different concentrations and plated in triplicates in a 96-well black wall plate. An excitation wavelength of 436 nm was used and emission at 690 was recorded, using an emission filter of 495 nm, to plot the fluorescence versus concentration graph.

Comparative photoacoustic studies for free SiNc(OH) and DFAC were performed using a Vevo 2100 LAZR system (Visualsonics, FujiFilm, ON) equipped with a 21 MHz transducer (LZ250) and an Nd:YAG laser. SiNc(OH) (stock prepared in DMSO) and DFACs were diluted in PBS at different concentrations and loaded in polyethylene tubes (BTPE-50; Instech Laboratories Inc., Plymouth Meeting, PA). Spectral photoacoustic measurements were performed in the wavelength range of 680 to 950 nm. PA signal intensity at 865 nm was used to plot the PA versus concentration graph post-adjustment of wavelength dependent laser output energy. PA imaging parameters—photoacoustic gain, laser power, signal intensity, and persistence were kept constant across different measurements. Image analysis was performed using the built-in VevoLab software. The effect of trypsin (Trypsin from bovine pancreas, Type I, ~10000 BAEE units/mg protein; MilliporeSigma, Burlington, MA) and Bovine serum albumin (BSA) (cold ethanol fraction, pH 5.2, ≥96%; MilliporeSigma, Burlington, MA) was studied by incubating the desired amount of DFAC with 0.1% Trypsin or BSA for 24 h at 37°C. To rule out the interference of temperature, all samples for this experiment were incubated for 24 h at 37°C. The samples were then imaged as described earlier. For studying the effect of DMSO, the DFAC or the free dye was appropriately diluted in DMSO and photoacoustic measurements were performed as described earlier.

Analyzing DFAC specificity.

EGFR expressing squamous cell carcinoma cells (A431) and the EGFR null Chinese hamster ovarian cell line (CHO) (obtained from ATCC, Manassas, VA) were cultured in DMEM (Fisher Scientific, Waltham, MA) and F-12K media (Thermo Fisher Scientific, Waltham, MA), respectively, supplemented with 10% FBS and antibiotic mixture containing Penicillin (100 I.U $mL^{-}1$) and streptomycin (100 μg $mL^{-}1$) (Mediatech, Inc., Manassas, VA). For DFAC specificity analysis, cells (5*103) were plated in a 96-well plate and cultured for 24 h. DFAC at different BPD equivalent concentrations (0.05, 0.1, 0.2, 0.25, 0.5, 1, and 2.5 μM) was added and incubated for 24 h. Cells were then fixed with 4% Paraformaldehyde (Electron Microscopy Sciences, Hatfield, PA), washed with phosphate-buffered saline, counterstained with Hoechst (Thermo Fisher Scientific, Waltham, MA) and

imaged using an Operetta CLS High-Content Analysis System (PerkinElmer, Waltham, MA). Image analysis was performed by the software provided by the manufacturer.

Preparation of cell encapsulating tissue phantom gelatin molds for fluorescence and photoacoustic imaging.

A431 and CHO cells were grown in a 150 mm Petri plate to confluency. DFACs were incubated with confluent cell cultures for 24 h, at a concentration of 2.5 μM SiNc (OH) dye equivalent. After incubation, cells were washed with PBS and scraped. Cells were counted and 10^7 cells were pelleted and resuspended in 100 μL PBS.

Preparation of tissue phantoms.

100 μL of 10% gelatin was added to a well of a 96-well plate and allowed to solidify. The gelatin base was made to minimize reverberations from the Petri dish bottom during PA imaging. Then 10^7 cells/100 μL PBS obtained previously were mixed with an equal volume of 10% gelatin and laid over the gelatin base in the 96-well plate to generate a tissue mimicking model as reported previously (42). The gelatin molds were allowed to solidify and imaged within 24 h.

Imaging of tissue phantoms.

Fluorescence imaging was performed using an IVIS® Lumina Series III In Vivo Imaging System (Perkin Elmer, Waltham, MA) using a 440 nm excitation filter and a 670 nm emission filter. Intensity calculations were performed using the Living Image® software provided by the manufacturer. PA imaging was performed by placing the 96-well plate in water. PA imaging parameters such as the photoacoustic gain, laser power, signal intensity, persistence, and frame rate were kept constant across different measurements. Image analysis was performed using the built-in software provided by Visualsonics, FujiFilm (ON, Canada).

In vitro Photo-toxicity of DFACs.

For phototoxicity studies, A431 and CHO cells were plated in 96-well plates at a cell density of 5000 cells per well. Cells were then treated with DFACs at a concentration of 250 nM BPD equivalent and incubated for a further 24 h. After incubation, media containing the DFAC were replaced with fresh media and cells were irradiated with energy densities ranging from 5 to 50 J $cm^{-}2$ at an irradiance of 150 mW $cm^{-}2$ irradiated using a 690 nm laser (Intense, Inc., North Brunswick, NJ). 24 h after irradiation, cells were assayed for viability by colorimetric MTT (3-(4,5-dimethylthiazol-2-yl)-2,5-diphenyltetrazolium bromide) (MilliporeSigma, Burlington, MA) assay. For determining the dose-dependent dark toxicity of DFAC, A431 cells were incubated with increasing concentration of DFAC (BPD equivalent, up to 5 μM) for 24 h. Cell viability was then monitored by MTT assay, as described previously.

Determining the intracellular localization of DFAC and mechanism of near infrared (NIR)-triggered cell death.

For determining the intracellular localization, A431 cells were plated in 35-mm glass bottom dishes (Cellvis, Mountain View, CA) at a cell density of 300 000 cells per dish and allowed to grow overnight at 37°C under 5% CO_2. The cells were then incubated with DFAC (1 μM BPD equivalent) for 24 h. Prior to fixing with Paraformaldehyde (4%), cells were incubated with 50 nM of MitoTracker™ Deep Red FM (Thermo Fisher Scientific, Waltham, MA) and 50 nM of LysoTracker™ Red DND-99 (Thermo Fisher Scientific, Waltham, MA) for 30 min prior. Cells were counterstained with Hoechst 33342 (Thermo Fisher Scientific, Waltham, MA) at a concentration of 1 μg mL^{-1} and visualized using an Olympus Fluoview FV1000 confocal laser scanning microscope (Olympus America, Center Valley, PA). Image analysis was performed using ImageJ software (National Institute of Health, Bethesda, MD). The mechanism of cell death was determined using the APC Annexin V Apoptosis Detection Kit with PI (BioLegend, San Diego, CA) as per the manufacturer's instructions. Briefly, A431 cells were incubated with DFAC (0.25 μM BPD) and irradiated as described earlier. After 24 h, cells were trypsinized and resuspended in Annexin V Binding Buffer followed by the addition of APC Annexin V and PI. The cells were then analyzed using a a flow cytometer (BD FACSAriaTM Cell Sorting System, Biosciences). Data analysis was performed using FlowJo software.

RESULTS

Synthesis of naphthalocyanine-derivative dye (SiNc(OH) and its NHS-derivative (SiNc(OH)-NHS)

The molecular structure and synthesis scheme of SiNc(OH)-NHS (compound **1**, Fig. 1) the naphthalocyanine-derivative dye, designed as the bioconjugatable contrast agent for photoacoustic imaging (PAI) in this study are shown in Fig. 1. SiNc(OH)-NHS is a silicon-centered naphthalocyanine chromophore with butoxy substituents at the α-positions. Octabutoxy-substituted silicon naphthalocyanine was chosen due to its absorbance at higher wavelengths (λ_{max} = 862 nm), stability, and synthetic accessibility (37,43). The central silicon was substituted with a hydroxyl group and an N-hydroxy succinimidyl ester coupled ether group. The N-hydroxy succinimidyl ester was coupled for the conjugation of SiNc(OH) to the cetuximab antibody. A siloxy (Si-O-Si) bonding group was used for the coupling of N-hydroxy succinimidyl as it resists hydrolysis, while Si-O-C bonds can be cleaved hydrolytically.

Synthesis of Dual function antibody conjugates (DFAC)

DFAC synthesis was performed as described in the reaction scheme (Fig. 2A). PEGylation of Cetuximab was performed to enhance DFAC solubility and minimize aggregation during and after conjugation of antibody to the hydrophobic dyes (BPD and SiNc(OH)). It is also known to enhance *in vivo* bioavailability by preventing antibody uptake by macrophages and minimizing protease-based antibody degradation (44-47). The crude DFAC mixture after the reaction was separated from the unreacted dyes by gel filtration, as it has been established in many previous studies from our group to eliminate any residual unreacted dye (45). The degree of labeling for BPD and SiNc(OH) was found to be 2.67 ± 0.16 and 3.01 ±

0.24 moles, per mole of Cetuximab, corresponding to a conjugation efficiency of 66.97 ± 4.05% and 75.36 ± 6.03%, for BPD and SiNc(OH), respectively. This is consistent with our previous studies with BPD where conjugation efficiency in the range of 45% to 75% have been reported for molar loading ratios between 10 and 2 BPD molecules per antibody (45). As shown in Fig. 2B, the absorption spectra of DFAC showed characteristic peaks at 690 and 865 nm, corresponding to the absorption maxima for the individual dyes.

Fluorescence and photoacoustic properties of DFAC

We further investigated the fluorescence and photoacoustic properties of DFAC to determine the effects of antibody conjugation on the fluorescence and photoacoustic signal of the two dyes, and to determine the range of concentrations over which the DFACs could be employed for multimodal imaging. As shown in Fig. 3A, BPD-based fluorescence in DFAC showed a linear increase ($R^2 = 0.9401$) with increase in concentration. The concentration-dependent fluorescence signal increase was similar to that observed for free BPD ($R^2 = 0.9384$), suggesting that DFACs, similar to BPD and other photoimmunoconjugates of BPD, can be used as molecular probes for fluorescence-based molecular imaging. The minimal spectral overlap between the two dyes (BPD and SiNc(OH)) (Fig. 2B) and the relatively low loading of BPD on Cetuximab meant that the homoquenching, usually observed for BPD conjugated PICs, with high BPD loading ratios (48), or a FRET-based heteroquenching of BPD, observed for conjugates having dyes with significant spectral overlap (49), was minimal. However, the slight decrease in fluorescence signals, observed for DFACs, as compared to the free BPD, could possibly be due to the above-mentioned reasons or antibody (protein)-based BPD fluorescence quenching.

In contrast to the fluorescence signals, PA signal amplitude from DFAC (Fig. 3B) was significantly attenuated as compared to that from the free SiNc(OH) dye (linear increase; $R^2 = 0.9673$). While the mechanistic details of PA signal attenuation upon antibody conjugation of SiNc(OH) are discussed later, our unpublished work with other PA dyes showed a similar decrease in PA signal intensity upon antibody conjugation, suggesting that it could be a general phenomenon associated with PA dyes-antibody/protein conjugates. These results suggest that fluorescence and photoacoustic signals of the dyes are retained, postconjugation on the Cetuximab antibody, and the proposed DFACs can be used for multimodal imaging over a wide range of concentrations, although with significantly attenuated photoacoustic signals.

Understanding PA signal attenuation upon Cetuximab conjugation

To gain mechanistic insights into the attenuation of PA signals of SiNc(OH) dye upon cetuximab conjugation, we studied the effect of (1) trypsinization and (2) solubilization of DFAC in DMSO. While trypsinization leads to degradation of the antibody molecules resulting in the generation of antibody fragments-dye conjugates, solubilization of DFAC in DMSO is expected to denature the antibody and minimize any noncovalent interactions between the dye and the protein. Interestingly, in our study trypsinization of DFAC led to a decrease in the PA signals (Fig. 4) of DFAC. Addition of BSA, used as a control, also resulted in a significant decrease in PA signals from DFAC. Addition of trypsin and BSA to the free SiNc(OH) dye also resulted in a significant reduction in PA signal.

These results suggest that the presence of protein molecules in the microenvironment of the dye leads to a reduction in PA signal, possibly due to the influence of proteins on solvent properties such as thermal diffusivity and Grüneisen parameters which are known to influence their acoustic properties (50,51). The absorption spectra of the free dye and DFAC were however not influenced by trypsin and BSA, at the concentrations tested (1 μM of dye; 0.1% BSA and trypsin) (Figure S1). In contrast, while DMSO had no effect on the PA signal of free SiNc(OH) dye, PA signal of DFAC significantly increased in DMSO, and was found to be approximately two-fold higher than that observed for free SiNc (OH) dye. Unlike, trypsinization which leads to cleavage of antibody molecules at specific sites and results in generation of peptide fragments which may still have the conjugated dye molecules, DMSO is known to denature proteins and minimize noncovalent interactions between drugs/dyes and antibody. The decrease in noncovalent interactions between the dye and antibody molecules could therefore be responsible for enhancing PA signal amplitude of DFAC in DMSO. Apart from this, the relatively lower specific heat capacity of DMSO (0.47 Cal/g/°C), as compared to water (1 Cal/g/°C), is also expected to have a major influence on PA signals (52). Importantly, the UV-Vis spectra for DFAC and free SiNc(OH) dye showed a significantly higher absorption at λmax (865 nm) upon solubilization in DMSO as compared to that in PBS (Figure S2), which could be yet another reason for increase in PA signal in DMSO as compared to PBS.

DFAC-based multimodal imaging of EGFR-overexpressing tumor cells

To monitor the specificity and multimodal imaging capability of DFAC, A431, and CHO cells were incubated with DFAC for 24 h (Fig. 5A). The squamous cell carcinoma cell line; A431 has a high expression of EGFR and is routinely used in studies related to EGFR-targeted therapeutics to establish specificity of the targeted agents. The Chinese Hamster Ovarian cell line; CHO was used as a negative control due to the lack of expression of human EGFR (53). Postincubation, cells were prepared (described in materials and methods) as depicted in Fig. 5B and imaged for fluorescence and photoacoustic signals. A431 cell phantoms (Fig. 5C lower panel) showed a significantly higher fluorescence intensity as compared to that of the CHO cell phantoms (Fig. 5C upper panel), which increased with the DFAC incubation time and concentration. Quantification of fluorescence intensities (Fig. 5D) indicated a significantly increased fluorescence intensity for A431 cell phantoms, incubated with DFAC for 24 h. However, CHO cell phantoms also showed fluorescence signals, possibly due to the nonspecific interactions due to the high concentration of the probe used for these experiments. Spectral photoacoustic measurements were performed to monitor SiNc(OH)-based PA signals from DFAC treated cells (Fig. 5E & F). A431 cell phantoms, in comparison to CHO cell phantoms, showed a higher PA signal which increased with DFAC incubation time and concentration. The fluorescence/PA signal observed for CHO cells treated with DFAC could possibly be due to nonspecific binding of DFAC at the high concentrations of DFAC used (2.5 μM SiNc(OH) equivalent), which was necessary to achieve detectable signals in PA measurements. A concentration of 1 μM (SiNc(OH) equivalent) showed significantly lower PA signal, even in A431 cells. To determine the specificity of DFAC, we treated A431 and CHO cells with increasing concentrations of DFAC followed by imaging the cells. As shown in Figure S3, DFAC fluorescence from CHO cells could be observed above a concentration of 0.2 μM (BPD equivalent),

corresponding to a cetuximab concentration of approximately 0.067 μM. However, the increase in fluorescence signal was significantly low for CHO cells (2% at 0.2 μM, 6.3% at 0.5 μM, 14.5 at 1 μM, and 35.65% at 2.5 μM) as compared to that from A431 cells (21.97% at 0.2 μM, 38.26% at 0.5 μM, 57.68% at 1 μM, and 116% at 2.5 μM) (Concentrations mentioned as BPD equivalent).

DFAC-based targeted dose-dependent phototoxicity in EGFR-overexpressing tumor cells

To validate the cell-specific phototoxicity conferred by DFAC, A431 and CHO cells were incubated with DFACs for 24 h followed by irradiation, with a 690 nm laser, at different light doses (0 to 50 J cm^{-2}) (Fig. 6A). As shown in Fig. 6B, A431 cells showed a dose-dependent toxicity with decrease in cell viability to 0.74 ± 0.17 (at 10 J cm^{-2}), 0.34 ± 0.12 (at 25 J cm^{-2}), and 0.21 ± 0.04 (at 50 J cm^{-2}). However, CHO cells were relatively unaffected by the DFAC and irradiation, showing a reduction in cell viability to 0.81 ± 0.16 at the highest light dose of 50 J cm^{-2}. These results suggest that DFAC can be used, apart from the imaging applications described above, for targeted photodynamic therapy of tumor cells.

To gain insights into the mechanism of cell death induced by photodynamic therapy (PDT) of DFAC-treated cells, Annexin V and PI staining followed by flow cytometry analysis was performed on untreated and DFAC-PDT treated cells. As shown in Fig. 6C (untreated) and 6D (DFAC-PDT treated A431 cells), DFAC-PDT treatment led to an increase in cell population in the late apoptotic (21.7%) and early apoptotic (13.3%) stage. The necrotic cell population, as suggested by Propidium Iodide (PI) only staining, of DFAC-PDT treated and control cells did not show much difference (2.28% and 3.08% for DFAC-PDT treated and untreated cells, respectively). These results suggest that the cytotoxic effect of DFAC-PDT is mediated mainly by apoptosis.

DISCUSSION

Molecular-targeted multimodal imaging is an important tool in cancer management with potential application in diagnostics and therapy guidance. Of all imaging modalities used in cancer management, fluorescence and photoacoustic imaging are two complementary techniques with a potential of real-time monitoring. An important application where multimodal imaging, enabled by fluorescence and photoacoustic imaging, can have potential impact is guidance, during surgical resection of tumors, to delineate tumor margins which is difficult to determine using current standard of care approaches. Given that there is evidence that attempts at re-resection of residual positive disease based on intraoperative frozen section does not result in local disease control rates equal to that of an initially negative resection, it is clear that the first cut is the most critical and it is here where image-guided tumor resections can have the greatest impact. Image-guided surgery is a common approach in the treatment for various cancer types (54), and more recently molecularly targeted constructs to enhance specificity during fluorescence-guided surgical resection have shown improvement over nontargeted fluorophores (26,55). While fluorescence-based tumor margin assessment is particularly popular due to its enhanced sensitivity owing to the high fluorescence quantum yield of most fluorophores, the use

of photosensitizers, with limited fluorescence quantum yields, may lead to a reduction in sensitivity. Moreover, as fluorescence measurements are limited in their depth profiling of solid tumors, complementing it with a spatially resolved imaging modality such as photoacoustic imaging, can to a great extent, enhance outcomes for margin assessment. In the present study, we demonstrate the feasibility of conjugation of two contrast agents, for fluorescence and PA imaging, simultaneously to the FDA approved anti-EGFR antibody (Cetuximab). The dual function antibody conjugates (DFACs) developed in this study can potentially enhance specificity and spatial resolution for image-guided surgeries. The utilization of a photosensitizer, Benzoporphyrin derivative (BPD), for its fluorescence properties also enables photoimmunotherapy of residual tumors (tumor bed sterilization), which otherwise recur, often with an aggressive phenotype.

Benzoporphyrin derivative (BPD) has been used frequently for imaging and therapy (48). Photoimmunoconjugates (PICs) developed by the conjugation of BPD to Cetuximab have been extremely successful in targeted imaging and treatment of both primary and metastatic tumors (38,48). However, the success has been more pronounced for tumors where the tumor size is limited to a few millimeters such as micro-metastatic ovarian cancer nodules (48), dimensions which are well within the optical diffusion limits of near infra-red light used for fluorescence-based measurements. In our present study, a strong BPD-based fluorescence signal was observed for DFAC treated A431 cell phantoms (Fig 5), as compared to the CHO cell phantoms, treated with DFAC. Although previous studies from our lab and others have shown much higher selectivity between EGFR positive and negative cells, the concentration of DFACs used in the present study, 2.5 μM SiNc(OH) equivalent, which corresponds to approximately 0.85 μM of Cetuximab, is significantly higher than previously utilized. A high concentration was used to enhance PA signal which is low due to (1) the low sensitivity of the instrument, and (2) attenuation of PA signal postconjugation to the antibody (Figs. 3B and 4). The fluorescence signals observed for CHO cell phantoms could therefore be due to nonspecific interactions between DFAC and CHO cells (Figure S3) at these high concentrations. Importantly, at these high concentrations, DFAC had no effect on cellular viability under dark conditions (Figure S4). Nevertheless, the information gained from fluorescence-based imaging in general and also described in the present study is superficial, representing 1-2 mm of the tissue. While the general advantage of fluorescence imaging in providing a wide-field view, also referred to as the “birds eye view” is accepted and assists in detection of small tumor extensions (otherwise not visible to the naked eye) away from the primary tumor site, its limitation in providing depth resolved images has long been realized. An efficient technique to overcome the limited depth profiling of fluorescence imaging, is photoacoustic imaging, which provides enhanced spatial resolution at depths well beyond the optical diffusion limit of fluorescence. In this context, naphthalocyanine-based dyes have found application in PA imaging, as sonochromes, due to their unique photophysical properties, characterized by a Q band in the NIR region and high extinction coefficients (37,56,57). Another advantage of using naphthalocyanine-based dyes is their NIR absorption properties which unlike other routinely used IR dyes (ICG, IRDye800, and Cy7), shows significantly low overlap with endogenous chromophores such as hemoglobin and melanin. However, the use of naphthalocyanine is hindered by their aggregation behavior which affects their photophysical properties and

distribution in biological systems. For this reason, modification of naphthalocyanine-based dyes to enhance their solubility while retaining their photophysical properties is important and has been reported in several studies. In this study, we report the modification of a naphthalocyanine-based dye; a silicon-centered octabutoxybenzopthalocyanine, as shown by Aoudia et *al.* (37), with improved solubility. An NHS group was introduced in the axial position of the octabutoxybenzopthalocyanine to mediate conjugation of the dye with Cetuximab antibody and hence improve specificity for molecular imaging. NHS ester units are among the most commonly used groups for bioconjugation (58). Axial substitution to the silicon center was preferred over peripheral substitutions due to its (1) ease of substitution and (2) disruption of aggregation in solution (37,59,60). The conjugation of two contrast agents to a single antibody, builds up on our previous work on conjugation of single fluorescent contrast agents, which has shown enhanced specificity in imaging and guiding therapies for various cancer types (48,61). Although the conjugation of SiNc(OH), in the present study, significantly compromised its PA intensity, our ongoing studies on identifying the mechanistic basis of this attenuation and synthesis of advanced naphthalocyanine dyes is expected to overcome this. Moreover, with the development of advanced clinical PA systems having imaging capability of a few centimeters, this is expected to improve further.

While the use of complementary imaging modalities is expected to enhance precision in tumor resection surgeries, a major reason for recurrence postsurgery is the residual microscopic disease. The use of photosensitizers as contrast agents for fluorescence imaging helps not only in surgical guidance but also in treatment of the residual microscopic disease through photodynamic activation of these photosensitizers. Photoimmunotherapy (PIT) has emerged as a promising tool for the treatment of various tumor types either alone or in combination with chemotherapy. This is exemplified by the recent clinical trials with PIT for head and neck cancers (62,63). As primary tumor may develop extensions off the main body of the tumor, it is necessary to resect a margin of 5 mm of healthy tissue adjacent to the tumor border in order to assure complete excision. This resection of marginal normal tissue clearly contributes to the compromise in function and appearance following oral cancer surgery. To address this challenge, we use the inherent theranostic capability of photosensitizers (in this case BPD) to achieve tumor-specific fluorescence contrast and also treat the surgical bed for any residual microscopic tumors that may have escaped the surgical resection procedure. This approach in theory both improves the likelihood of a complete surgical resection using the intraoperative guidance provided and also treats the microscopic residual disease remaining. This combination will allow for a more precise and complete excision with minimal resection of normal tissue, preserving postoperative function. As shown in Fig. 6, the phototoxicity achieved is specific to EGFR expressing cells and is predominantly mediated by mitochondrial and lysosomal localization of the photosensitizer and induction of apoptosis (64,65) (Fig. 6 and Figure S5). Moreover, as the treatment is envisaged on the surgical bed, post-tumor resection, it overcomes the light penetration issue often encountered in PDT-based treatment strategies (66). In this context, encouraging results have been reported by Moore *et al.*, using fluorescence-based resection and PDT of residual tumor in preclinical head and neck cancer models (34).

While the present study provides the basis for development of imaging probes with dual imaging and treatment capabilities, all in one molecular-targeted construct, there are several

short-comings which have to be addressed for its translation to clinical settings; (1) A major hurdle is the compromise in PA signal amplitude observed after the conjugation of SiNc(OH) dye to the Cetuximab antibody. Our unpublished work with other PA dyes suggests that this could be a general phenomenon associated with PA dye conjugation to antibody/proteins and the effect of the microenvironment on photophysical properties of PA dyes. (2) Recent studies have suggested that ROS generated through PS irradiation could lead to photodegradation of PA dyes (67), thereby compromising their function. As it is envisaged that the probe may be used for imaging (PA and fluorescence) followed by photodynamic therapy, there is minimal possibility of reactive oxygen species (ROS) mediated photodamage to PA SiNc(OH). Importantly, no significant changes in PA signal intensity of SiNc(OH) dye were observed while performing a forward scan (680–970 nm), where the photosensitizer is excited first (at 690 nm) as compared to a reverse scan (970–680 nm), where the PA measurements from SiNc(OH) are performed first (Figure S6). (3) Finally, the biocompatibility of the naphthalocyanine dyes has to be evaluated for their approval by regulatory authorities and translation to the clinic.

To summarize, our study puts forward a case for an imaging probe with a molecular targeted multimodal imaging capability to identify tumor margins during tumor resection surgeries. Moreover, the use of a photosensitizer in the probe further adds to its utility for treating the surgical tumor bed with photoimmunotherapy (PIT) to treat any residual microscopic tumor which if untreated leads to recurrence.

Supplementary Material

Refer to Web version on PubMed Central for supplementary material.

Acknowledgements—

This work was supported by grants from National Institute of Health P01 CA084203, R01 CA231606, S10OD012326, R21 CA220143 to TH.

REFERENCES

1. Zhao J, Chen J, Ma S, Liu Q, Huang L, Chen X, Lou K and Wang W (2018) Recent developments in multimodality fluorescence imaging probes. Acta Pharmaceutica Sinica B 8, 320–338. [PubMed: 29881672]
2. Kang N-Y, Lee JY, Lee SH, Song IH, Hwang YH, Kim MJ, Phue WH, Agrawalla BK, Wan SYD and Lalic J (2020) Multimodal imaging probe development for pancreatic β cells: From fluorescence to PET. J. Am. Chem. Soc 142, 3430–3439. [PubMed: 32040300]
3. Martí-Bonmatí L, Sopena R, Bartumeus P and Sopena P (2010) Multimodality imaging techniques. Contrast Media Molecular Imaging 5, 180–189. [PubMed: 20812286]
4. Hernot S, van Manen L, Debie P, Mieog JSD and Vahrmeijer AL (2019) Latest developments in molecular tracers for fluorescence image-guided cancer surgery. Lancet Oncol. 20, e354–e367. [PubMed: 31267970]
5. Weissleder R and Pittet M (2008) Imaging in the era of molecular oncology. Nature 452, 580–589. [PubMed: 18385732]
6. Zhang HF, Maslov K, Stoica G and Wang LV (2006) Functional photoacoustic microscopy for high-resolution and noninvasive in vivo imaging. Nat. Biotechnol 24, 848–851. [PubMed: 16823374]

7. Maeda A, Bu J, Chen J, Zheng G and DaCosta RS. (2015) Dual in vivo photoacoustic and fluorescence imaging of HER2 expression in breast tumors for diagnosis, margin assessment, and surgical guidance. Mol. Imaging 14. 10.2310/7290.2014.00043
8. Mallidi S, Luke GP and Emelianov S (2011) Photoacoustic imaging in cancer detection, diagnosis, and treatment guidance. Trends Biotechnol. 29, 213–221. [PubMed: 21324541]
9. Hester SC, Kuriakose M, Nguyen CD and Mallidi S (2020) Role of ultrasound and photoacoustic imaging in photodynamic therapy for cancer. Photochem. Photobiol 96, 260–279. [PubMed: 31919853]
10. Barth CW and Gibbs SL (2020) Fluorescence image-guided surgery: a perspective on contrast agent development. Molecular-Guided Surgery: Molecules, Devices, and Applications VI 11222, 112220J.
11. Attia ABE, Balasundaram G, Moothanchery M, Dinish U, Bi R, Ntziachristos V and Olivo M (2019) A review of clinical photoacoustic imaging: Current and future trends. Photoacoustics 16, 100144. [PubMed: 31871888]
12. Tummers QR, Hoogstins CE, Peters AA, de Kroon CD, Trimbos JBM, van de Velde CJ, Frangioni JV, Vahrmeijer AL and Gaarenstroom KN (2015) The value of intraoperative near-infrared fluorescence imaging based on enhanced permeability and retention of indocyanine green: feasibility and false-positives in ovarian cancer. PLoS One 10, e0129766. [PubMed: 26110901]
13. Hadjipanayis CG, Widhalm G and Stummer W (2015) What is the surgical benefit of utilizing 5-aminolevulinic acid for fluorescence-guided surgery of malignant gliomas? Neurosurgery 77, 663–673. [PubMed: 26308630]
14. Matsumura Y and Maeda H (1986) A new concept for macro-molecular therapeutics in cancer chemotherapy: Mechanism of tumoritropic accumulation of proteins and the antitumor agent smancs. Can. Res 46, 6387–6392.
15. Kelloff GJ, Krohn KA, Larson SM, Weissleder R, Mankoff DA, Hoffman JM, Link JM, Guyton KZ, Eckelman WC and Scher HI (2005) The progress and promise of molecular imaging probes in oncologic drug development. Clin. Cancer Res 11, 7967–7985. [PubMed: 16299226]
16. Liu Y, Nie L and Chen X (2016) Photoacoustic molecular imaging: from multiscale biomedical applications towards early-stage theranostics. Trends Biotechnol. 34, 420–433. [PubMed: 26924233]
17. Yao J and Wang LV (2018) Recent progress in photoacoustic molecular imaging. Curr. Opin. Chem. Biol 45, 104–112. [PubMed: 29631120]
18. Weber J, Beard PC and Bohndiek SE (2016) Contrast agents for molecular photoacoustic imaging. Nat. Methods 13, 639–650. [PubMed: 27467727]
19. Ledermann J, Canevari S and Thigpen T (2015) Targeting the folate receptor: Diagnostic and therapeutic approaches to personalize cancer treatments. Ann. Oncol 26, 2034–2043. [PubMed: 26063635]
20. Maennling AE, Tur MK, Niebert M, Klockenbring T, Zeppernick F, Gattenlöhner S, Meinhold-Heerlein I and Hussain AF (2019) Molecular targeting therapy against EGFR family in breast cancer: Progress and future potentials. Cancers 11, 1826. [PubMed: 31756933]
21. Mallidi S, Kim S, Karpiouk A, Joshi PP, Sokolov K and Emelianov S (2015) Visualization of molecular composition and functionality of cancer cells using nanoparticle-augmented ultrasound-guided photoacoustics. Photoacoustics 3, 26–34. [PubMed: 25893171]
22. Capala J and Bouchelouche K (2010) Molecular imaging of HER2-positive breast cancer-a step toward an individualized “Image and Treat” strategy. Curr. Opin. Oncol 22, 559–566. [PubMed: 20842031]
23. Kramer L, Renko M, Završnik J, Turk D, Seeger MA, Vasiljeva O, Grütter MG, Turk V and Turk B (2017) Non-invasive in vivo imaging of tumour-associated cathepsin B by a highly selective inhibitory DARPin. Theranostics 7, 2806. [PubMed: 28824717]
24. Xavier M-A-E, Liu S, Bugge TH, Torres JB, Mosley M, Hopkins SL, Allen PD, Berridge G, Vendrell I and Fischer R (2019) Tumor imaging using radiolabeled matrix metalloproteinase-activated anthrax proteins. J. Nucl. Med 60, 1474–1482. [PubMed: 30954944]

25. Crisp JL, Savariar EN, Glasgow HL, Ellies LG, Whitney MA and Tsien RY (2014) Dual targeting of integrin αvβ3 and matrix metalloproteinase-2 for optical imaging of tumors and chemotherapeutic delivery. Mol. Cancer Ther 13, 1514–1525. [PubMed: 24737028]
26. Rosenthal EL, Warram JM, De Boer E, Chung TK, Korb ML, Brandwein-Gensler M, Strong TV, Schmalbach CE, Morlandt AB and Agarwal G (2015) Safety and tumor specificity of cetuximab-IRDye800 for surgical navigation in head and neck cancer. Clin. Cancer Res 21, 3658–3666. [PubMed: 25904751]
27. Tummers WS, Miller SE, Teraphongphom NT, Gomez A, Steinberg I, Huland DM, Hong S, Kothapalli S-R, Hasan A and Ertsey R (2018) Intraoperative pancreatic cancer detection using tumor-specific multimodality molecular imaging. Ann. Surg. Oncol 25, 1880–1888. [PubMed: 29667116]
28. Tummers WS, Miller SE, Teraphongphom NT, van den Berg NS, Hasan A, Longacre TA, Fisher GA, Bonsing BA, Vahrmeijer AL and Gambhir SS (2019) Detection of visually occult metastatic lymph nodes using molecularly targeted fluorescent imaging during surgical resection of pancreatic cancer. HPB (Oxford) 21, 883–890. [PubMed: 30723062]
29. Miller SE, Tummers WS, Teraphongphom N, van den Berg NS, Hasan A, Ertsey RD, Nagpal S, Recht LD, Plowey ED and Vogel H (2018) First-in-human intraoperative near-infrared fluorescence imaging of glioblastoma using cetuximab-IRDye800. J. Neurooncol 139, 135–143. [PubMed: 29623552]
30. Yamamoto Y, Kodama K, Maniwa T and Takeda M (2017) Surgical resection of advanced non-small cell lung cancer after a response to EGFR-TKI: presentation of two cases and a literature review. J. Cardiothor. Surg 12, 98.
31. van Manen L, Handgraaf HJ, Diana M, Dijkstra J, Ishizawa T, Vahrmeijer AL and Mieog JSD (2018) A practical guide for the use of indocyanine green and methylene blue in fluorescence-guided abdominal surgery. J. Surg. Oncol 118, 283–300. [PubMed: 29938401]
32. Schipmann S, Müther M, Stögbauer L, Zimmer S, Brokinkel B, Holling M, Grauer O, Molina ES, Warneke N and Stummer W (2020) Combination of ALA-induced fluorescence-guided resection and intraoperative open photodynamic therapy for recurrent glioblastoma: case series on a promising dual strategy for local tumor control. J. Neurosurg 1, 1–11.
33. De Silva P, Saad MA, Thomsen HC, Bano S, Ashraf S and Hasan T (2020) Photodynamic therapy, priming and optical imaging: potential co-conspirators in treatment design and optimization. J. Porphyrins Phthalocyanines 24, 1320–1360.
34. Moore LS, de Boer E, Warram JM, Tucker MD, Carroll WR, Korb ML, Brandwein-Gensler MS, van Dam GM and Rosenthal EL (2016) Photoimmunotherapy of residual disease after incomplete surgical resection in head and neck cancer models. Cancer Med. 5, 1526–1534. [PubMed: 27167827]
35. Firey P and Rodgers M (1987) Photo-properties of a silicon naphthalocyanine: A potential photosensitizer for photodynamic therapy. Photochem. Photobiol 45, 535–538. [PubMed: 3575445]
36. Cuomo V, Jori G, Rihter B, Kenney M and Rodgers M (1991) Tumour-localising and-photosensitizing properties of liposome-delivered Ge (IV)-octabutoxy-phthalocyanine. Br. J. Cancer 64, 93. [PubMed: 1854632]
37. Aoudia M, Cheng G, Kennedy VO, Kenney ME and Rodgers MA (1997) Synthesis of a series of octabutoxy-and octabutoxy-benzophthalocyanines and photophysical properties of two members of the series. JACS 119, 6029–6039.
38. Nath S, Saad MA, Pigula M, Swain JW and Hasan T (2019) Photoimmunotherapy of ovarian cancer: a unique niche in the management of advanced disease. Cancers 11, 1887. [PubMed: 31783651]
39. Saad M, Xavierselvan M, Sharif HA, Mallidi S and Hasan T. (2019) Dual function antibody conjugates (DFACs) for drug quantification and therapy (Conference Presentation). Vol. 11070, pp. 1107011. International Society for Optics and Photonics, Proceedings of the 17th International Photodynamic Association World Congress2019.
40. Mallidi S, Saad MA, Pawle R, Xavierselvan M, Takiff L and Hasan T (2021) NIR dye antibody conjugates for molecular photoacoustic imaging and photodynamic therapy. pp. OTu3D. 3.

Optical Society of America, Proceedings of the Optical Molecular Probes, Imaging and Drug Delivery2021.

41. Oleinick NL, Antunez AR, Clay ME, Rihter BD and Kenney ME (1993) New phthalocyanine photosensitizers for photodynamic therapy. Photochem. Photobiol 57, 242–247. [PubMed: 8451285]
42. Mallidi S, Larson T, Aaron J, Sokolov K and Emelianov S (2007) Molecular specific optoacoustic imaging with plasmonic nanoparticles. Opt. Express 15, 6583–6588. [PubMed: 19546967]
43. Cook MJ, Dunn AJ, Howe SD, Thomson AJ and Harrison KJ (1988) Octa-alkoxy phthalocyanine and naphthalocyanine derivatives: dyes with Q-band absorption in the far red or near infra-red. J. Chem. Soc. Perkin Transac 1, 2453–2458.
44. Savellano MD and Hasan T (2005) Photochemical targeting of epidermal growth factor receptor: A mechanistic study. Clin. Cancer Res 11, 1658–1668. [PubMed: 15746071]
45. Savellano MD and Hasan T (2003) Targeting cells that overexpress the epidermal growth factor receptor with polyethylene glycolated BPD verteporfin photosensitizer immunoconjugates¶. Photochem. Photobiol 77, 431–439. [PubMed: 12733655]
46. Chapman AP (2002) PEGylated antibodies and antibody fragments for improved therapy: A review. Adv. Drug Deliv. Rev 54, 531–545. [PubMed: 12052713]
47. Villaraza AJL, Milenic DE and Brechbiel MW (2010) Improved speciation characteristics of PEGylated indocyanine green-labeled Panitumumab: Revisiting the solution and spectroscopic properties of a near-infrared emitting anti-HER1 antibody for optical imaging of cancer. Bioconjug. Chem 21, 2305–2312. [PubMed: 21073171]
48. Spring BQ, Abu-Yousif AO, Palanisami A, Rizvi I, Zheng X, Mai Z, Anbil S, Sears RB, Mensah LB and Goldschmidt R (2014) Selective treatment and monitoring of disseminated cancer micrometastases in vivo using dual-function, activatable immunoconjugates. Proc. Natl Acad. Sci 111, E933–E942. [PubMed: 24572574]
49. Obaid G, Spring BQ, Bano S and Hasan T (2017) Activatable clinical fluorophore-quencher antibody pairs as dual molecular probes for the enhanced specificity of image-guided surgery. J. Biomed. Optics 22, 121607.
50. Oraevsky AA, Jacques SL and Tittel FK (1997) Measurement of tissue optical properties by time-resolved detection of laser-induced transient stress. Appl Opt. 36, 402–415. [PubMed: 18250688]
51. Shah J, Park S, Aglyamov SR, Larson T, Ma L, Sokolov KV, Johnston KP, Milner TE and Emelianov SY (2008) Photoacoustic imaging and temperature measurement for photothermal cancer therapy. J. Biomed. Optics 13, 34024.
52. Mahmoodkalayeh S, Jooya HZ, Hariri A, Zhou Y, Xu Q, Ansari MA and Avanaki MR (2018) Low temperature-mediated enhancement of photoacoustic imaging depth. Sci. Rep 8, 1–9. [PubMed: 29311619]
53. Shi W, Fan H, Shum L and Derynck R (2000) The tetraspanin CD9 associates with transmembrane TGF-α and regulates TGF-α-induced EGF receptor activation and cell proliferation. J. Cell. Biol 148, 591–602. [PubMed: 10662783]
54. Parrish-Novak J, Holland EC and Olson JM (2015) Image guided tumor resection. Cancer J. 21, 206–212. [PubMed: 26049700]
55. Zhang RR, Schroeder AB, Grudzinski JJ, Rosenthal EL, Warram JM, Pinchuk AN, Eliceiri KW, Kuo JS and Weichert JP (2017) Beyond the margins: Real-time detection of cancer using targeted fluorophores. Nat. Rev. Clin. Oncol 14, 347. [PubMed: 28094261]
56. Zhang Y and Lovell JF (2017) Recent applications of phthalocyanines and naphthalocyanines for imaging and therapy. Wiley Inter-disc. Rev. Nanomed. Nanobiotechnol 9, e1420.
57. Duffy MJ, Planas O, Faust A, Vogl T, Hermann S, Schafers M, Nonell S and Strassert CA (2018) Towards optimized naphthalocyanines as sonochromes for photoacoustic imaging in vivo. Photoacoustics 9, 49–61. [PubMed: 29707479]
58. Kalia J and Raines RT (2010) Advances in bioconjugation. Curr Organ. Chem 14, 138–147.
59. Li Z, Huang X, Xu S, Chen Z, Zhang Z, Zhang F and Kasatani K (2007) Effect of aggregation on nonlinear optical properties of a naphthalocyanine. J. Photochem. Photobiol., A 188, 311–316.

60. Wheeler BL, Nagasubramanian G, Bard AJ, Schechtman LA and Kenney ME (1984) A silicon phthalocyanine and a silicon naphthalocyanine: synthesis, electrochemistry, and electrogenerated chemiluminescence. J. Am. Chem. Soc 106, 7404–7410.

61. Soukos NS, Hamblin MR, Keel S, Fabian RL, Deutsch TF and Hasan T (2001) Epidermal growth factor receptor-targeted immunophotodiagnosis and photoimmunotherapy of oral precancer in vivo. Can. Res 61, 4490–4496.

62. Gillenwater AM, Cognetti D, Johnson JM, Curry J, Kochuparambil ST, McDonald D, Fidler MJ, Stenson K, Vasan N and Razaq M (2018) RM-1929 photo-immunotherapy in patients with recurrent head and neck cancer: Results of a multicenter phase 2a open-label clinical trial. J. Clin. Oncol 36, 6039. 10.1200/JCO.2018.36.15_suppl.6039

63. Cognetti D, Curry JM, Gillenwater AM, William WN, Kochuparambil ST, McDonald D, Fidler M, Stenson KM, Vasan NR and Razaq MA (2018) A phase 2a, multicenter, open-label study of RM-1929 photoimmunotherapy in patients with recurrent head and neck cancer. Int. J. Radiat. Oncol. Biol. Phys 100, 1368.

64. Kessel D and Oleinick NL (2018) Cell death pathways associated with photodynamic therapy: an update. Photochem. Photobiol 94, 213–218. [PubMed: 29143339]

65. Celli JP, Solban N, Liang A, Pereira SP and Hasan T (2011) Verteporfin-based photodynamic therapy overcomes gemcitabine insensitivity in a panel of pancreatic cancer cell lines. Lasers Surg. Med 43, 565–574. [PubMed: 22057484]

66. Momma T, Hamblin MR, Wu HC and Hasan T (1998) Photodynamic therapy of orthotopic prostate cancer with benzoporphyrin derivative: local control and distant metastasis. Can. Res 58, 5425–5431.

67. Petrovic LZ, Xavierselvan M, Kuriakose M, Kennedy MD, Nguyen CD, Batt JJ, Detels KB and Mallidi S (2020) Mutual impact of clinically translatable near-infrared dyes on photoacoustic image contrast and in vitro photodynamic therapy efficacy. J. Biomed. Optics 25, 63808.

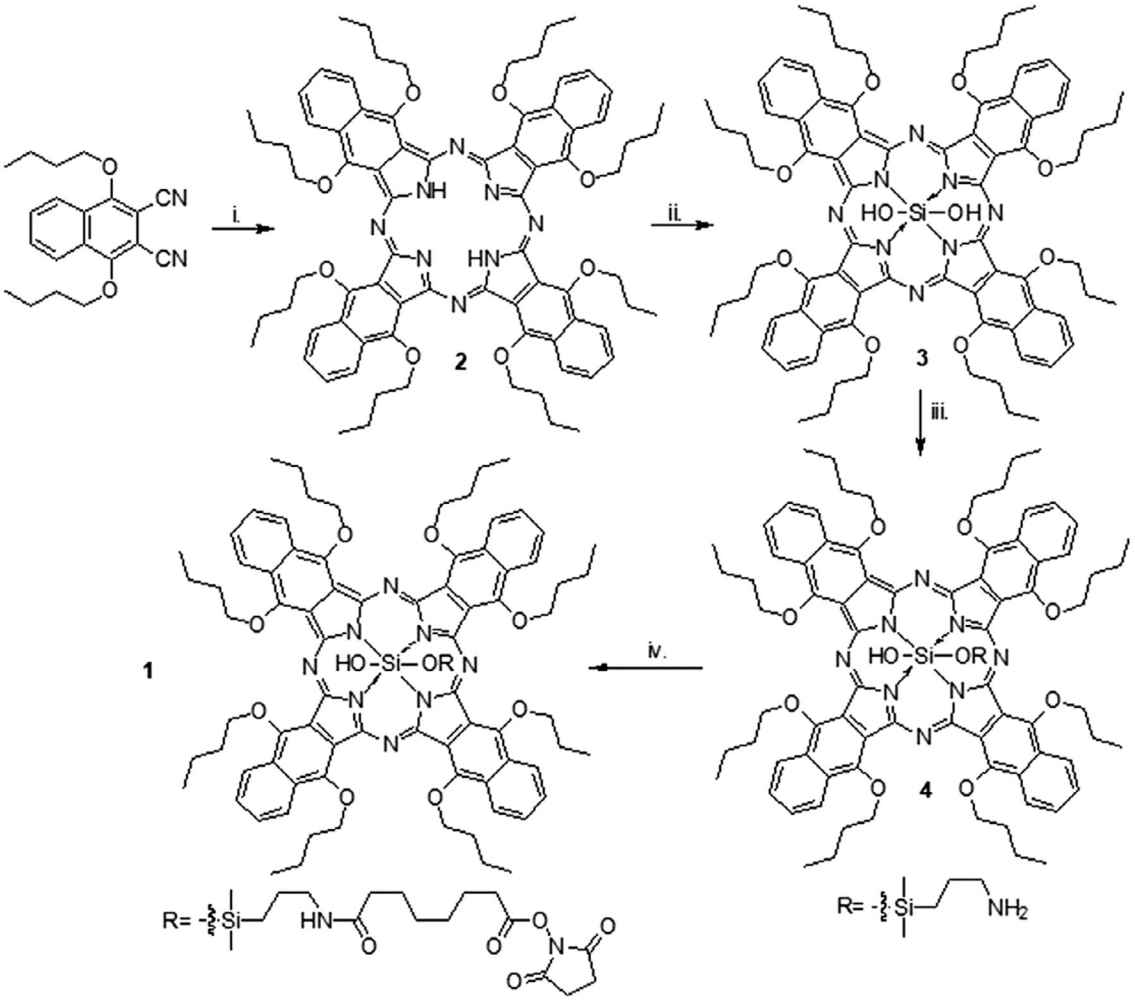

Figure 1.

Schematic representation of preparation of compound 1 (SiNc(OH)-NHS), as described in materials and methods. i. Li, *n*-butanol, 130°C, 20.2%. ii. (1) Trichlorosilane, $N(C_4H_9)_3$, CH_2Cl_2, RT. (2) $N(C_2H_5)_3$, H_2O, RT, 69.4%. iii. 3-aminopropyldimethylmethoxysilane, pyridine, 160°C, 34.1%. iv. Suberic acid, bis(*N*-hydroxy succinimidyl ester), CH_2Cl_2, RT, 50.5%.

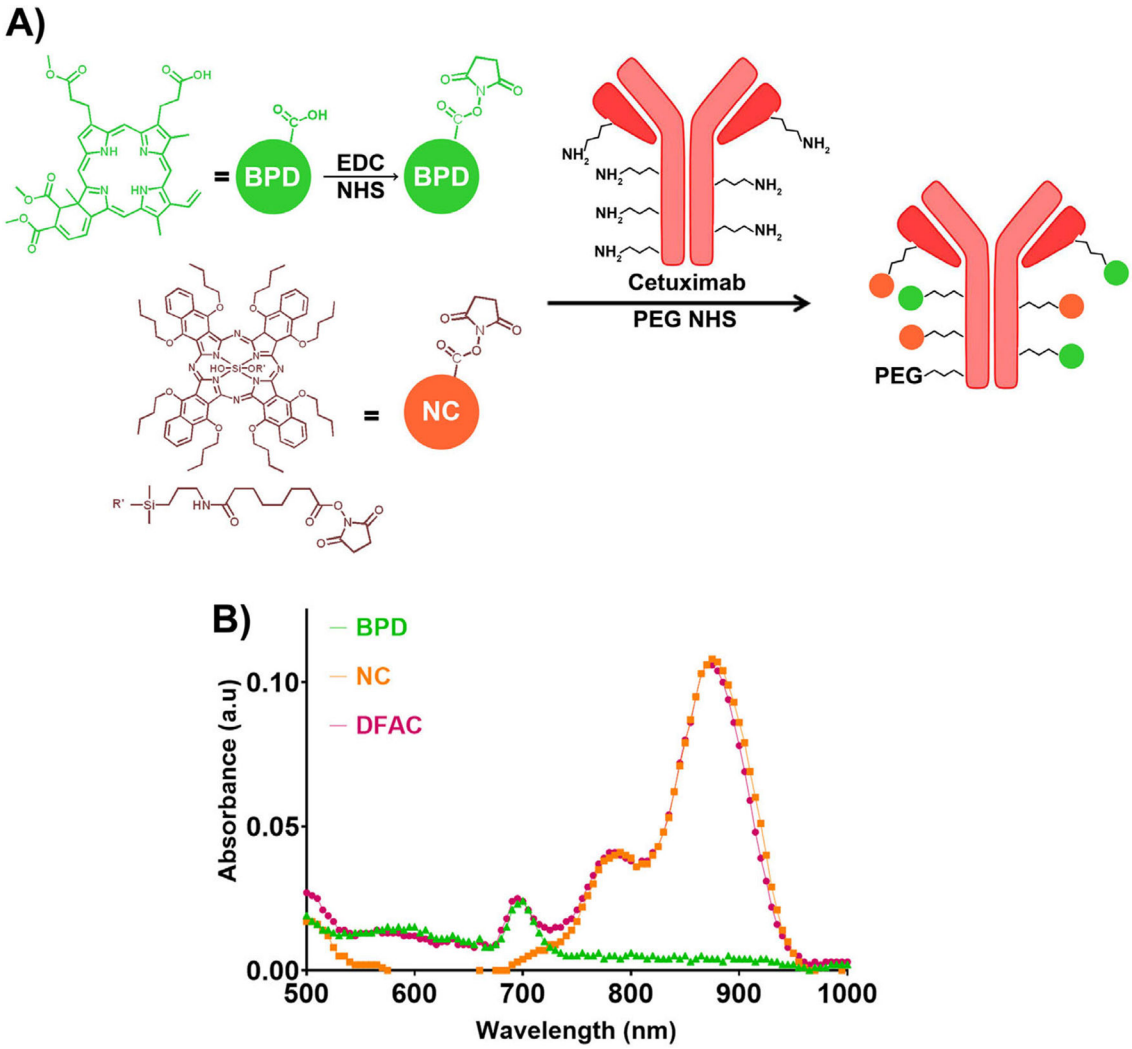

Figure 2.

(A) Synthesis of dual function antibody conjugates (DFACs); BPD was reacted with EDC/NHS to generate the respective amine-reactive N-hydroxysuccinimidyl derivative. The NHS esters of BPD and SiNc(OH) (prepared as described in Fig. 1) were then reacted with Cetuximab antibody, previously reacted with an N-hydroxysuccinimidyl derivative of PEG. The resulting DFAC had approximately 1 PEG molecule, and 3 molecules each of BPD and SiNc(OH). (B) Absorption spectra of BPD (shown in green triangles), SiNc(OH) (shown in orange squares) and DFAC (shown in red circles). DFAC showed characteristic peaks corresponding to the absorption of the individual dyes.

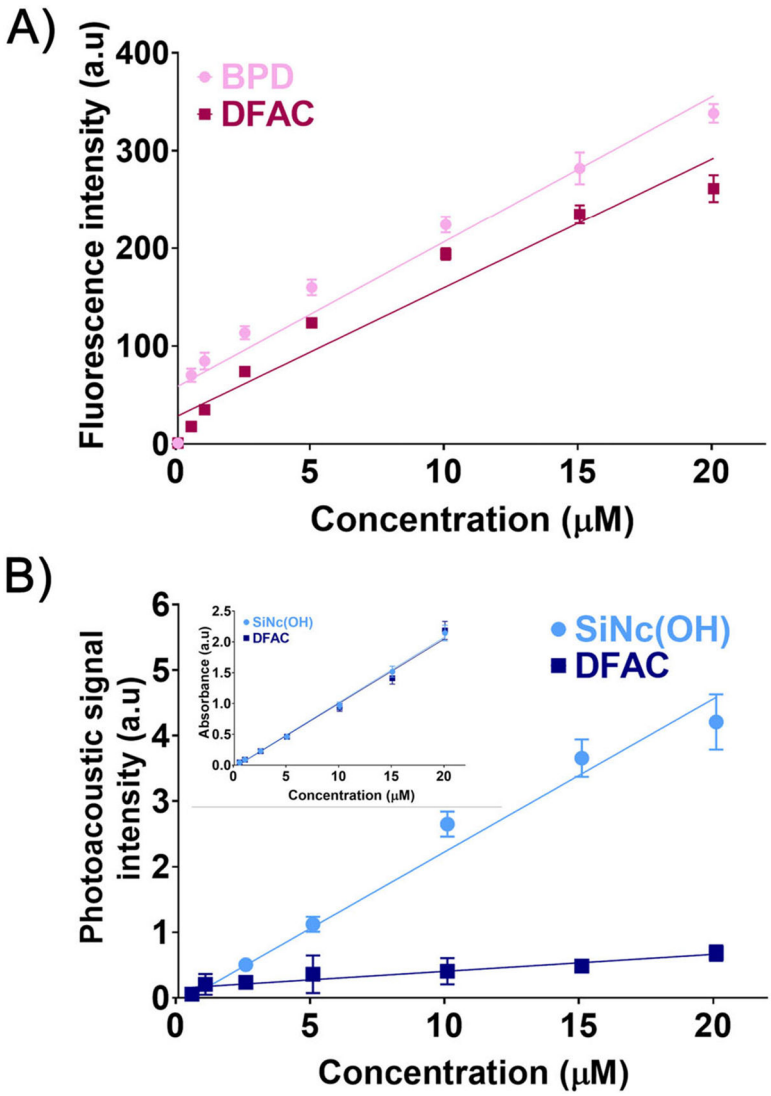

Figure 3.

(A) BPD fluorescence from free BPD (pink circles) and DFAC (red circles). Linear trend lines with R^2 values of 0.9401 and 0.9384 for BPD and DFAC suggest a linear increase in fluorescence signal with concentration. (B) Photoacoustic intensity of SiNc(OH) (light blue circles) and DFAC (dark blue circles) with increasing concentration. Although a linear increase for both free SiNc(OH) (R^2 = 0.9673) and DFAC (R^2 = 0.6315) was observed, the PA signal intensity from DFACs was significantly attenuated. Inset in Fig. B shows absorbance at 865 nm for SiNc(OH) and DFAC as a function of concentration in PBS. The absorption at 865 nm for free SiNc(OH) and DFAC were found to be similar at all the concentrations tested.

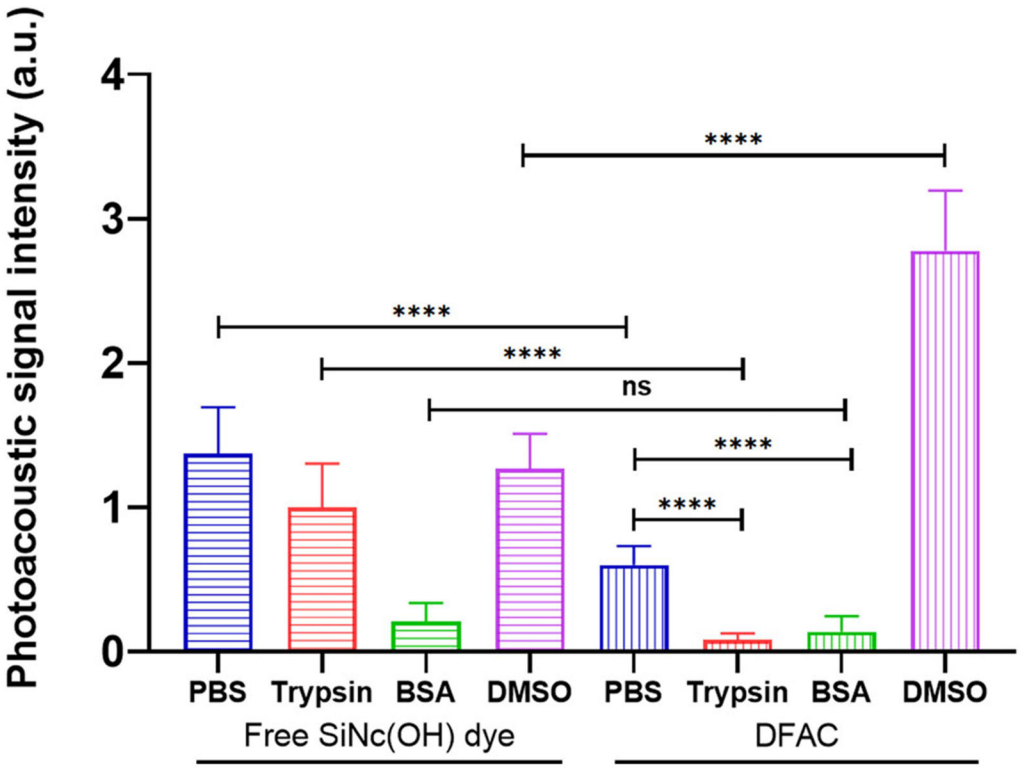

Figure 4.

Effects of trypsinization and DMSO solubilization on PA signal of DFAC. While free SiNc(OH) dye showed decrease in PA signal amplitude in the presence of Trypsin and BSA, DMSO had no significant effect on the PA signal. In contrast, the PA signal from DFAC was significantly reduced in PBS as compared to that from the free dye. While trypsinization and addition of BSA led to a significant decrease in PA signal from DFAC, solubilization of DFAC in DMSO led to a significant increase in PA signal. All measurements were performed in the indicated solvent at SiNc(OH) equivalent concentration of 5 μM. Trypsin and BSA-based studies were performed in PBS. Data are presented as mean ± S.D ($n \geq 3$), analyzed using one-way ANOVA with Tukey's test for post hoc analysis. *P*-values < 0.05 were considered to be significant and are indicated by asterisks as follows: $^{ns}P > 0.05$, $^{*}P < 0.05$, $^{**}P < 0.01$, $^{***}P < 0.001$ and $^{****}P < 0.0001$.

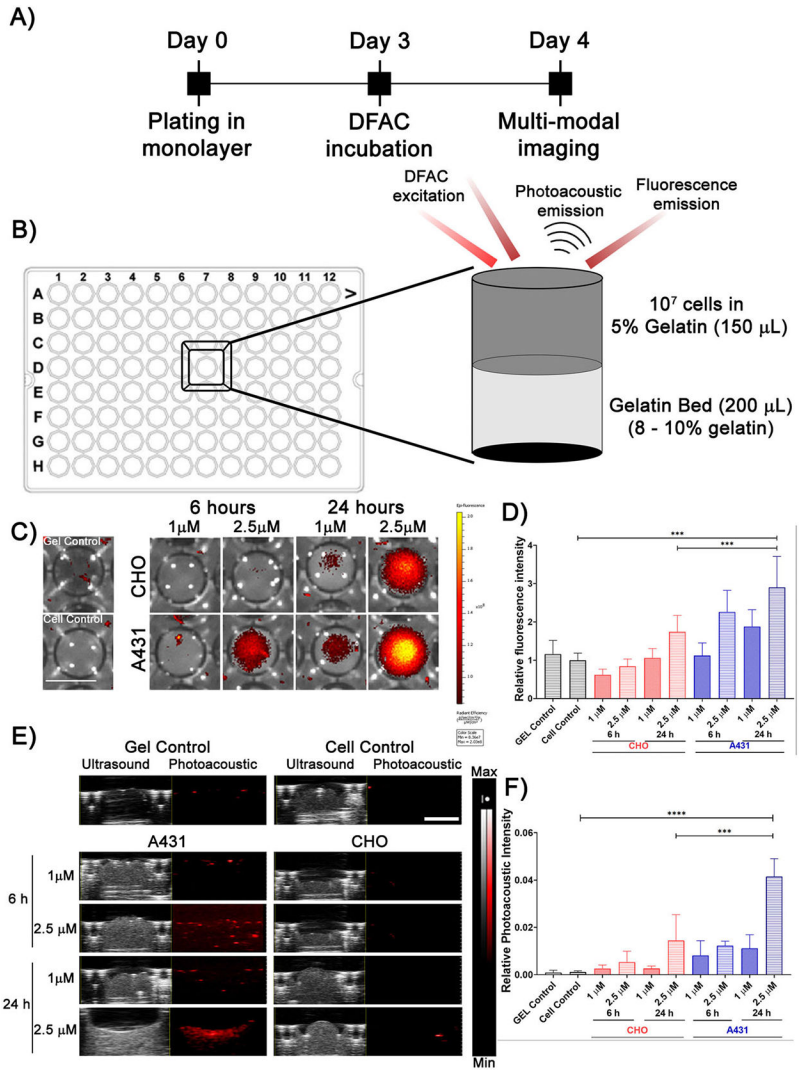

Figure 5.

(A) Experimental timeline for DFAC-based *in vitro* multimodal imaging. (B) Experimental setup for preparing phantoms for multimodal imaging. (C) IVIS imaging of the DFAC treated (2.5 µM SiNc(OH) equivalent) A431 and CHO cells prepared as gelatin embedded tissue mimicking phantoms in a 96-well plate (Scale bar = 5 mm). (D) Quantification of fluorescence signals from the IVIS images. A431 cells showed significantly higher fluorescence signal with a 24 h DFAC incubation as compared to CHO cells. (E) Ultrasound and photoacoustic images (865 nm wavelength illumination) of the DFAC treated A431 and CHO phantoms. (F) Photoacoustic signal quantification showed a significant increase in PA signal from A431 cells as compared to CHO cells. Scale bar corresponds to 2 mm. For 5D and 5F data are presented as mean ± SD ($n \geq 3$), analyzed using one-way ANOVA with Tukey's test for post hoc analysis. *P*-values < 0.05 were considered to be significant and are indicated by asterisks as follows: $^{ns}P > 0.05$, $^{*}P < 0.05$, $^{**}P < 0.01$, $^{***}P < 0.001$ and $^{****}P < 0.0001$.

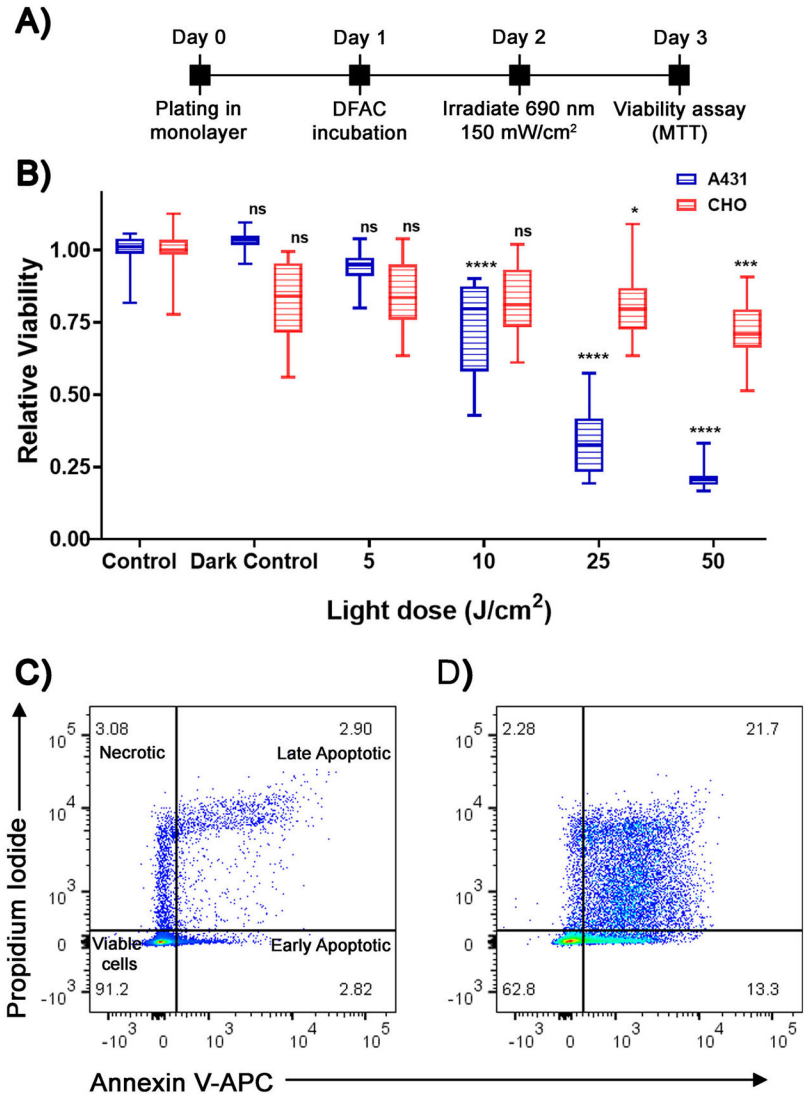

Figure 6.

(A) Experimental timeline for DFAC-based (0.25 μM BPD equivalent) *in vitro* phototoxicity studies in A431 and CHO cell lines. (B) Relative viability of A431 and CHO cells treated with different light doses. A431 showed a significant decrease in cell viability at a light dose of 10 J cm^{-2} and above. The viability of CHO cells was unaffected even at the highest (50 J cm^{-2}) light dose. Data are presented as mean ± SD ($n \geq 12$), analyzed using one-way ANOVA with Dunnett's test for post hoc analysis. *P*-values < 0.05 were considered to be significant and are indicated by asterisks as follows: $^{ns}P > 0.05$, $*P < 0.05$, $**P < 0.01$, $***P < 0.001$ and $****P < 0.0001$. (C and D) APC Annexin V and PI staining of control (C) and DFAC-PDT (D) treated A431 cells. DFAC-PDT treatment resulted in a significantly higher percentage of cells in the early and late apoptotic stage. The necrotic population was similar between the control and DFAC-PDT treated cells, suggesting that apoptosis is the major mechanism of cell death.